Title

Bright, Mechanosensitive Upconversion with Cubic-Phase Heteroepitaxial Core–Shell Nanoparticles

Journal

Nano Letters, 18(7)

ISSN

1530-6984

Authors

Lay, Alice
Siefe, Chris
Fischer, Stefan
et al.

Publication Date

2018-07-11

DOI

10.1021/acs.nanolett.8b01535

Peer reviewed

NANO LETTERS
Letter
Cite This: Nano Lett. 2018, 18, 4454−4459
pubs.acs.org/NanoLett

Bright, Mechanosensitive Upconversion with Cubic-Phase Heteroepitaxial Core−Shell Nanoparticles

Alice Lay,*[,†] Chris Siefe,[‡] Stefan Fischer,[‡] Randy D. Mehlenbacher,[‡] Feng Ke,[§] Wendy L. Mao,[§] A. Paul Alivisatos,[∥,⊥,#,▽] Miriam B. Goodman,[○] and Jennifer A. Dionne*[,‡]

[†]Department of Applied Physics, [‡]Department of Materials Science and Engineering, and [§]Department of Geological Sciences, Stanford University, Stanford, California 94305, United States

[∥]Department of Chemistry and [⊥]Department of Materials Science and Engineering, University of California, Berkeley, California 94720, United States

[#]Materials Sciences Division, Lawrence Berkeley National Laboratory, Berkeley, California 94720, United States

[▽]Kavli Energy NanoScience Institute, Berkeley, California 94720, United States

[○]Department of Molecular and Cellular Physiology, Stanford University, Stanford, California 94305, United States

Supporting Information

ABSTRACT: Lanthanide-doped nanoparticles are an emerging class of optical sensors, exhibiting sharp emission peaks, high signal-to-noise ratio, photostability, and a ratiometric color response to stress. The same centrosymmetric crystal field environment that allows for high mechanosensitivity in the cubic-phase (α), however, contributes to low upconversion quantum yield (UCQY). In this work, we engineer brighter mechanosensitive upconverters using a core−shell geometry. Sub-25 nm α-$NaYF_4$:Yb,Er cores are shelled with an optically inert surface passivation layer of ∼4.5 nm thickness. Using different shell materials, including $NaGdF_4$, $NaYF_4$, and $NaLuF_4$, we study how compressive to tensile strain influences the nanoparticles' imaging and sensing properties. All core−shell nanoparticles exhibit enhanced UCQY, up to 0.14% at 150 W/cm^2, which rivals the efficiency of unshelled hexagonal-phase (β) nanoparticles. Additionally, strain at the core−shell interface can tune mechanosensitivity. In particular, the compressive Gd shell results in the largest color response from yellow-green to orange or, quantitatively, a change in the red to green ratio of 12.2 ± 1.2% per GPa. For all samples, the ratiometric readouts are consistent over three pressure cycles from ambient to 5 GPa. Therefore, heteroepitaxial shelling significantly improves signal brightness without compromising the core's mechano-sensing capabilities and further, promotes core−shell cubic-phase nanoparticles as upcoming in vivo and in situ optical sensors.

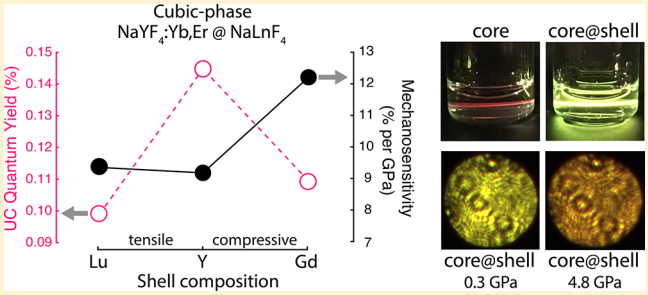

KEYWORDS: *Heteroepitaxial, core−shell, upconversion, lanthanides, quantum yield, mechanosensitivity*

Small optical probes are highly sought after for biological imaging and sensing applications. Currently, most probes rely on labeling with dyes and fluorescent proteins or inorganic options like quantum dots.[1] However, these probes typically suffer from signal instability and high background noise from excitation in the visible or ultraviolet wavelengths. Upconverting nanoparticles (UCNPs) are a promising class of optical probes due to excitation in the near-infrared and subsequent emission in the visible, tunability, and photostability.[2] Typical hosts are ceramic sodium rare-earth tetrafluoride materials, which have two main crystal structures: the cubic-phase (α) and hexagonal-phase (β). While hexagonal-phase nanoparticles are generally brighter and therefore more well-studied in the field, an emerging advantage of the cubic-phase nanoparticles is their optical response to a variety of stimuli,[3] including mechanical forces,[4,5] temperature,[6−9] and magnetic fields.[10] Our group previously demonstrated that UCNPs have a color response to applied stress quantified by a linear change in the red to green emission ratio $\left(\frac{I_r}{I_g}\right)$. The centrosymmetric crystal field of the cubic-phase yields high mechanosensitivity that is at least 2× that of optimized hexagonal-phase nanoparticles.[4] Ironically, the high crystal symmetry also contributes to their low quantum yield (QY), which remains a challenge for implementing them in material and biological systems.

Shelling is a common technique used to improve the efficiency of UCNPs by passivating the surface and reducing surface quenching.[11] Surface quenching processes include nonradiative losses through defects, dangling bonds, ligands,

Received: April 17, 2018
Revised: June 4, 2018
Published: June 21, 2018

DOI: 10.1021/acs.nanolett.8b01535
Nano Lett. 2018, 18, 4454−4459

and more.[12,13] Shells above 4 nm in thickness provide significant upconversion quantum yield (UCQY) enhancement of up to 57× on ~20 nm hexagonal-phase cores at 63 W/cm^2.[14] Deciding which type of material to use as a shell is critical because it directly influences the nanoparticles' growth, emission properties, and compatibility to external environments. Several groups, for example, have used alkaline earth metal fluoride (e.g., CaF_2),[15−17] metallic,[18] and silica[19] shells to enhance upconversion efficiency and/or improve biocompatibility. Shell layers can also introduce multimodal imaging properties beyond luminescence, allowing for applications in computed tomography (CT) and magnetic resonance imaging (MRI).[20] Meanwhile, Johnson and van Veggel identified the effect of shelling with a lattice-mismatched material (i.e., heteroepitaxial growth) on morphology; they found that tensile strain led to highly isotropic nanoparticles in contrast to compressive strain.[21] As growth is affected, it is likely that optical and sensing properties are too. It has been shown that compressive shells in quantum dots, for example, alter the conduction and valence band energies, leading to shifts in emission.[22] To date, however, it has not been well-studied how the range of compressive and tensile strain influences both the optical and sensing properties in lanthanide core−shell nanoparticles.

In this work, we investigate the effect of heteroepitaxial shelling on upconversion emission properties, QY, and sensitivity to mechanical stress. We synthesize a series of nanoparticles with strain at the core−shell interface. Specifically, we utilize $NaYF_4$ as the core's host material and $NaGdF_4$ and $NaLuF_4$ as materials for compressive and tensile strain in the shell, respectively. Through effective surface passivation, the UCQY of sub-25 nm upconverting α-$NaYF_4$:Yb,Er cores are improved by nearly 2 orders of magnitude. This value is comparable to those reported for similar-sized unshelled hexagonal-phase nanoparticles.[23] Minimal strain is optimal for QY and does not alter the inherently high mechanosensitivity of cubic-phase cores. On the other hand, nanoparticles with compressive shells actually have improved mechanosensitivity and yield a color response from yellow-green to orange under applied stress. Our core−shell design therefore leverages the mechano-sensing capabilities of the cubic-phase lattice and optimizes upconversion efficiency for practical use as an in vivo or in situ tool.

The schematic in Figure 1a summarizes our study, which details the effects of an inert α-$NaLnF_4$ (Ln = Gd, Y, or Lu) shell on an upconverting α-$NaYF_4$ core doped with 18% Yb^{3+} and 2% Er^{3+}. $NaGdF_4$ has a larger lattice constant and therefore, must be compressed to fit the Y-based core, while $NaLuF_4$ experiences tension. Following one-pot colloidal procedures for cubic-phase nanoparticles,[24] we synthesize ~30 nm core−shell nanoparticles. First, the cores are synthesized in a large 250 mL flask with 1 mmol Ln^{3+}, so that all shells are grown on a common core and better comparisons can be made across core−shell samples. The cores have average diameters of 23.2 ± 3.5 nm. Transmission electron micrographs (TEMs) in Figure 1b−d show the monodispersity of our quasi-spherical core−shell nanoparticles, which have average diameters of 29.6 ± 2.3 nm (Gd), 32.1 ± 2.3 nm (Y), and 32.2 ± 3.9 nm (Lu). Therefore, shell thicknesses are ~4.5 nm, though the inert Gd shell is slightly smaller at ~3.2 nm. Gd is typically a more difficult material to grow on a Y host due to the negative lattice mismatch; even at just a few nanometers thick, Gd-shelling can yield anisotropy

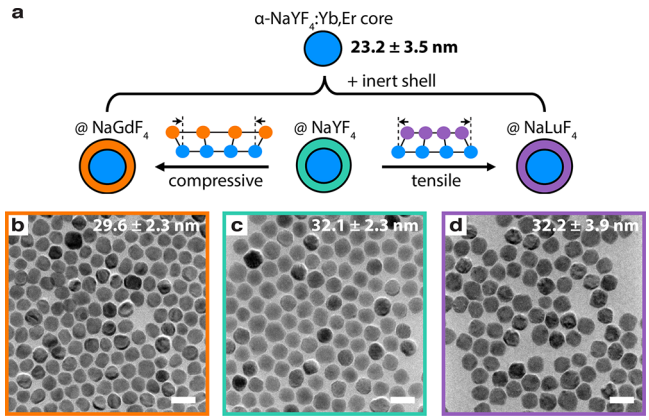

Figure 1. Schematic and micrographs of core−shell nanoparticles. (a) We shell upconverting cores with different materials to study the effects of compressive and tensile strain at the core−shell interface. In the presence of a lattice mismatch, we expect the shell to experience strain in order to conform to the core much like heteroepitaxial thin film growth. With varied lanthanide ionic radii, we can access compressive to tensile strain, using an inert Gd shell (orange), an inert Y shell (teal), and an inert Lu shell (purple). (b−d) TEMs show the quasi-spherical morphology and monodispersity of synthesized nanoparticles. Average sizes or diameters are listed in the top right corner. The scale bar is 50 nm.

and polydispersity.[21] Lastly, for a control we create a sample in which the shell is of the same material composition as the core, α-$NaYF_4$:Yb,Er. This shell is considered optically active due to the presence of sensitizer Yb^{3+} and emitter Er^{3+} ions in the shell. Additional details on the syntheses, particle size analysis, and chemical composition are located in the Supporting Information (SI).

We characterize the structural properties of our nanoparticles using X-ray diffraction (XRD). Figure 2a shows that

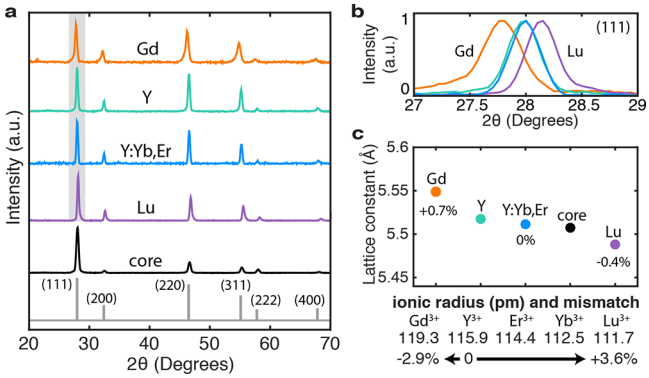

Figure 2. Structural characterization and induced strain. (a) X-ray diffraction peaks for core and core−shell samples, acquired using a Cu Kα_1 source (λ = 1.54056 Å). α-$Na_{0.39}Y_{0.61}F_{2.22}$ (ICDD 04-019-9099) serves as the reference structure for shelled nanostructures. (b) A zoom-in of the (111) diffraction peak shows a shift in the 2θ angle position, broadening, and asymmetry for strained Gd-shelled (orange) and Lu-shelled (purple) samples compared to the unstrained Y-shelled (teal) and Y:Yb,Er-shelled (blue) samples. (c) Effective lattice parameters of core−shell nanoparticles are consistent with the differences between the lanthanides' ionic radii. An inert Gd shell expands the lattice by 0.7%, whereas a Lu inert shell decreases the overall lattice by 0.4%. Below, we list the ionic radius of lanthanide ions from Gd^{3+} to Lu^{3+}. Per conventions in literature, the negative (positive) sign indicates compressive (tensile) strain at the shell.

DOI: 10.1021/acs.nanolett.8b01535
Nano Lett. 2018, 18, 4454−4459

the diffraction peaks for core and core−shell nanostructures match cubic-phase materials of space group $Fm\text{-}3m$ and zinc blende crystal structure. Changes in the relative intensities of those peaks indicate a stoichiometric change from core to all core−shell nanostructures from α-$Na_{0.29}Y_{0.71}F_{1.57}$ to α-$Na_{0.39}Y_{0.61}F_{2.22}$. As a result, we compare the samples relative to the control sample with the active Y:Yb,Er shell (blue) and match it to the α-$Na_{0.39}Y_{0.61}F_{2.22}$ reference, ICDD 04-019-9099, plotted in gray.

A closer look at individual diffraction peaks reveals evidence for synthetically induced strain. In Figure 2b, for example, a zoom-in of the (111) crystallite highlights a peak shift toward smaller 2θ angles for the Gd-shelled nanoparticles and larger 2θ angles for the Lu-shelled nanoparticles. Smaller 2θ angles are associated with larger d-spacings, corresponding to Gd^{3+} having a larger ionic radius compared to Y^{3+} by 2.9%. The reverse is true for Lu^{3+} with a mismatch of 3.6%. In addition, the asymmetric shape of diffraction peaks for the Gd- and Lu-shelled nanoparticles likely result from a superposition of lattice spacings and, therefore, a strain gradient. Such inhomogeneous strain is not surprising. Analogous to epitaxial growth in thin films or quantum dots, strain will be greatest in magnitude at the core−shell interface then decay over at least a few atomic layers.[21,25] Hence, the Gd-shelled sample has a longer tail toward lower angles, whereas the opposite is true for the Lu-shelled sample. According to the Lennard-Jones potential,[26,27] there is a smaller energy barrier for tensile strain to occur compared to compressive strain. Thus, the higher degrees of asymmetry and broadening detected in Gd-shelled nanoparticles likely result from the core lattice stretching in response to the compressive shell. Finally, we Pawley-fit the diffraction peaks to extract an effective lattice constant (Figure 2c). The inert Y shell, active shell, and core have similar lattice constants of 5.52, 5.51, and 5.51 Å, respectively. In contrast, an inert Gd shell increases the lattice constant by 0.7% to 5.55 Å, whereas an inert Lu shell decreases the parameter by 0.4% to 5.49 Å. For reference, α-$Na_5Gd_9F_{32}$ (ICDD 00-027-0698) has a lattice constant of 5.59 Å, and α-$Na_5Lu_9F_{32}$ (ICDD 00-027-0725) has a lattice constant of 5.46 Å. Given that the shell comprises ∼30% (Gd) or ∼40% (Lu) of the total volume, we can estimate the lattice parameter of the core−shell composite as 5.54 Å (Gd) or 5.49 Å (Lu). This calculation is consistent with our experimental results.

Beyond structural changes, shelling has a prominent effect on the nanoparticles' optical properties. This change can be qualitatively seen in spectral measurements and quantified using QY measurements. First, we compare the spectra of cores (black) and Y-shelled UCNPs (teal), as seen in Figure 3a. The inset demonstrates this enhancement qualitatively, even though the core sample is 2× more concentrated than the Y-shelled sample. In the pictures and spectral measurements, nanoparticles are suspended in cyclohexane and illuminated with a 980 nm diode laser at ∼10 W/cm^2 and 150 W/cm^2, respectively. Quite noticeably, the color from core to core−shell changes from red to yellow. This is due to the relative enhancement of the green emission peaks (520 and 545 nm) compared to the red emission peak (660 nm). Because our eyes are more sensitive to green light, a red to green ratio $\frac{I_r}{I_g} > 1$ can have a perceived yellow-green emission color. The change in color is not so much a consequence of the surface passivation, but rather size and a stoichiometric shift during the shelling procedure (Figure 2a). In Figure 3b, for example, the

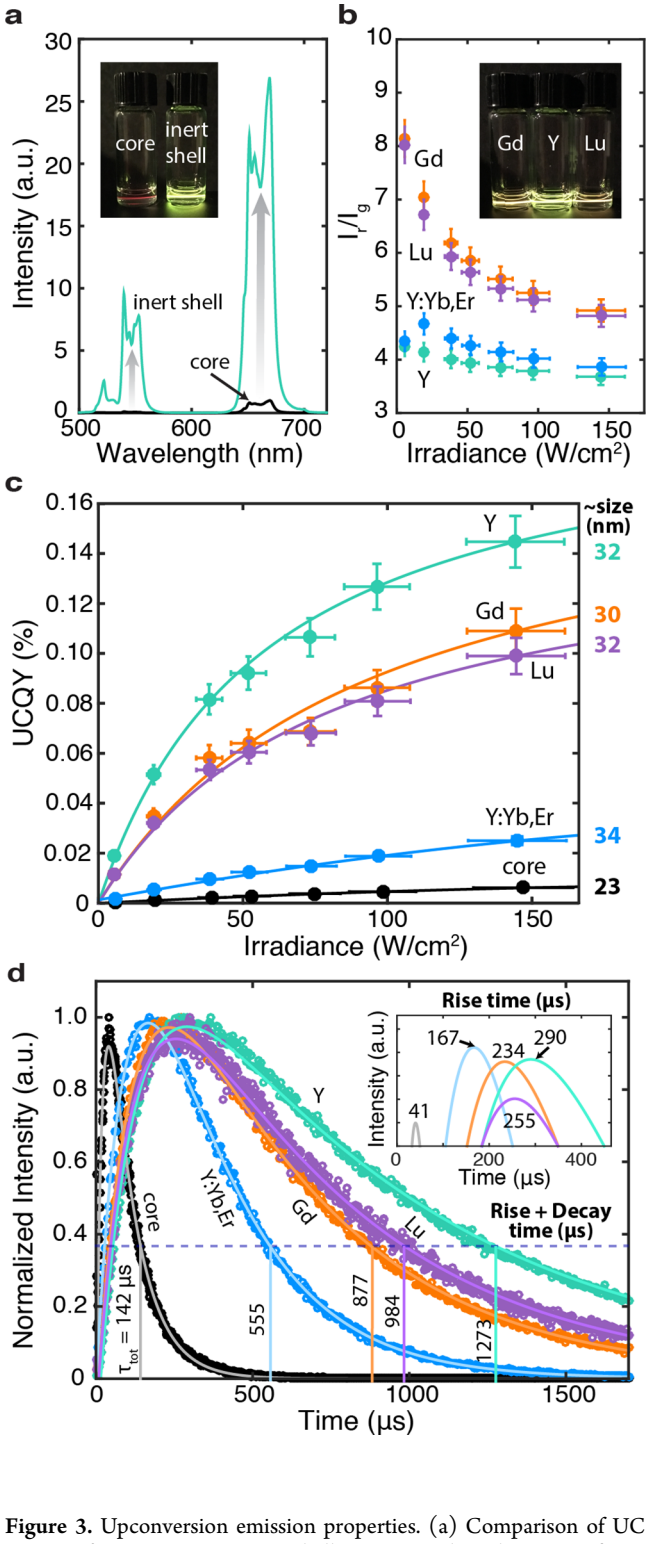

Figure 3. Upconversion emission properties. (a) Comparison of UC spectra from core to core−shell nanoparticles show significant enhancement in intensity at 150 W/cm^2 despite 2× more concentrated cores. Inset: nanoparticles suspended in cyclohexane under 980 nm illumination at ∼10 W/cm^2. (b) Red to green emission ratio, $\frac{I_r}{I_g}$, of core−shell samples over two magnitudes of irradiance values. In the inset, the Gd- and Lu-shelled samples appear redder than the Y-shelled sample at low powers. (c) Quantum yield of samples over two magnitudes of irradiance values. Here, guides-to-the-eye and average particle sizes (diameters) are added to highlight trends. (d) Lifetime curves showing the rise and total (τ_{tot} = rise + decay) time of red emission (654 nm) under 980 nm excitation.

DOI: 10.1021/acs.nanolett.8b01535
Nano Lett. 2018, 18, 4454−4459

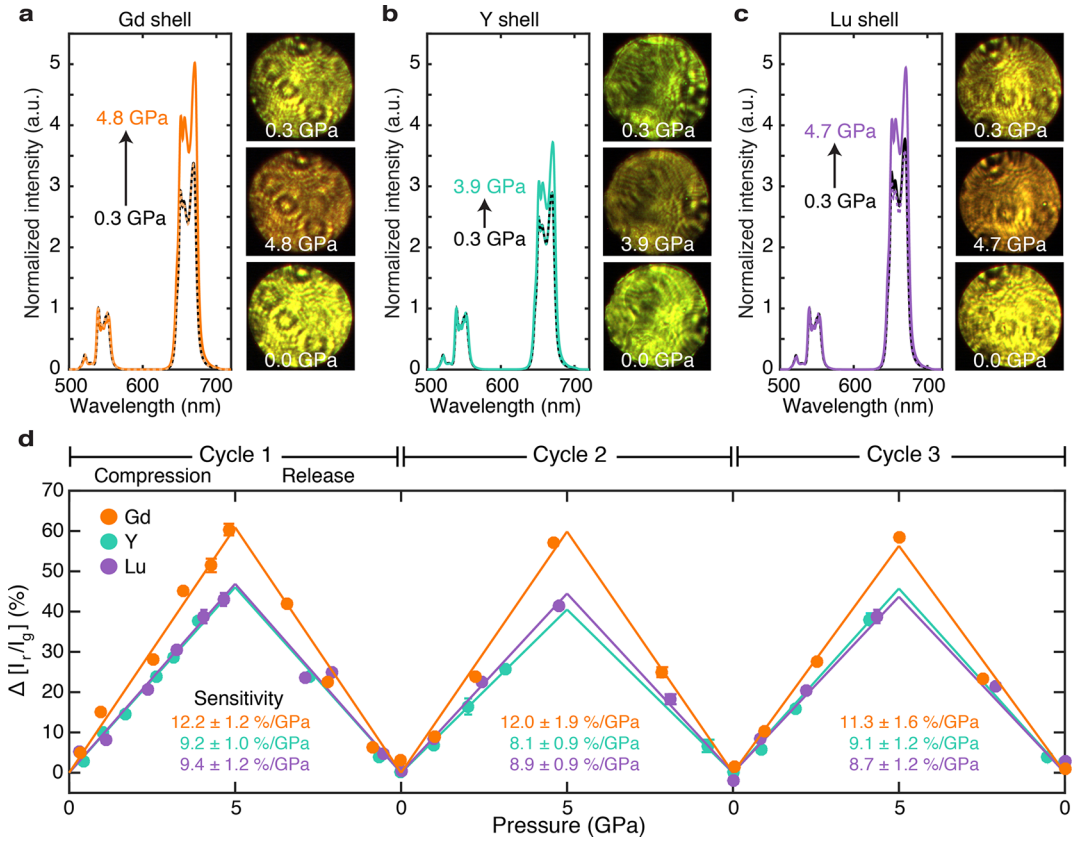

Figure 4. Mechanosensitivity or color response of core−shell UCNPs. UC spectra at the loading (black), maximum (color), and full release (dashed color) pressures for (a) Gd-, (b) Y-, and (c) Lu-shelled UCNPs. Each spectrum is normalized to its green emission peak to see the relative change in red emission. Arrows indicate the increase in red emission upon compression. Side-by-side optical images of the DAC sample chamber (~295 μm in diameter) qualitatively show the corresponding UC intensity and color changes. (d) DAC measurements spanning 3 complete compression and release cycles for the three core−shell nanoparticle types. Error bars represent the standard deviation of $\frac{I_r}{I_g}$ values, derived from three spectra collected at each pressure point. Note that the error bars may lie within markers. Error-weighted linear fits of each pressure cycle are graphed. Their slopes are labeled and represent the mechanosensitivity or quantitative color change, $\Delta\frac{I_r}{I_g}$ (% per GPa).

active Y:Yb,Er shell (blue) does not benefit from surface passivation and yields a similar red to green ratio as the Y inert shell, $\frac{I_r}{I_g} \approx 4$ at 150 W/cm^2. Within the shelled series, we see that the red to green ratios across two orders of irradiance values are 1.25−2× higher for the strained inert Gd (orange) and Lu (purple) shells versus the unstrained Y and Y:Yb,Er shells. The inset shows those qualitative color differences of UCNPs at equal concentrations, suspended and illuminated in solution. We explain these color differences in the context of lifetime measurements in the SI. Briefly, strained shells increase the probability of nonradiative decay, which impact the green and red emission unequally.

We measure the QY of these colloidally suspended nanoparticles over a wide range of irradiance. In the SI, we provide details on the integrating sphere setup and down-shifting process (i.e., NIR QY). Here, we focus on UCQY, defined as the ratio of emitted red and green photons over the number of absorbed photons. In Figure 3c, we record 24-fold enhancement in UCQY or efficiencies of 0.14 ± 0.01% using an inert Y shell compared to the core (6.1 ± 0.5 × 10^{-3}%) at 150 W/cm^2. Interestingly, the samples undergoing synthetic strain have slightly lower UCQY efficiencies of 0.11 ± 0.01% (Gd) and 0.10 ± 0.01% (Lu). While this decrease could partially be explained by the smaller average size of Gd-shelled UCNPs, the same explanation is not applicable to the Lu-shelled UCNPs. In fact, we expect strained shells to have more nonradiative decay pathways. We compare the inert shells to our active Y:Yb,Er-shelled sample, which has an average diameter of 33.6 ± 1.9 nm and provides only 6× improvement over the cores. In addition, we investigate the dependence of core size on UCQY; larger cores of ~27 nm provide only 2× enhancement (further details in SI). Hence, the enhancements from an inert shell layer cannot be merely explained by increased size and differences introduced by the shelling procedure.

Figure 3d provides insight into the mechanism by which the inert shell improves efficiency. NIR to visible upconversion is a nonlinear multiphoton process that relies on long-lived lifetimes for population of higher energetic states.[11] We excite the nanoparticle system with 980 nm and track the population (rise time) and depopulation (decay time) of key Er^{3+} energetic states. Specifically, the plot shows normalized lifetime curves for red emission ($^4F_{9/2} \rightarrow {}^4I_{15/2}$) under nanosecond pulsed 980 nm excitation. Note that measured lifetimes encompass both radiative and nonradiative (e.g., phononic) pathways. Surface passivation increases nonradiative lifetimes by making it less likely for fast decay processes to occur, thereby increasing total lifetimes in both the population and depopulation of states. As seen in the inset, rise times increase

DOI: 10.1021/acs.nanolett.8b01535
Nano Lett. 2018, 18, 4454−4459

Table 1. Summary of Structural, Optical, and Sensing Properties for Core−Shell UCNPs

sample	diameter (nm)	stoichiometry from XRD	lattice constant (Å)	red to green ratio at 150 W/cm^2	UCQY at 150 W/cm^2 (%)	980 nm → 654 nm decay lifetime (μs)	mechanosensitivity $\Delta\frac{I_r}{I_g}$ (%/GPa)
core	23.2 ± 3.5	$Na_{0.29}Y_{0.71}F_{1.57}$	5.51	23.87 ± 1.01	6.1 ± 0.5 × 10^{-3}	101	
Y:Yb,Er-shelled	33.6 ± 1.9	$Na_{0.39}Y_{0.61}F_{2.22}$	5.51	3.86 ± 0.16	2.5 ± 0.2 × 10^{-2}	88	
Y-shelled	32.1 ± 2.3	$Na_{0.39}Y_{0.61}F_{2.22}$	5.52	3.68 ± 0.16	0.14 ± 0.01	983	9.2 ± 1.0
Gd-shelled	29.6 ± 2.3	$Na_{0.39}Y_{0.61}F_{2.22}$	5.55	4.92 ± 0.21	0.11 ± 0.01	643	12.2 ± 1.2
Lu-shelled	32.2 ± 3.9	$Na_{0.39}Y_{0.61}F_{2.22}$	5.49	4.82 ± 0.20	0.10 ± 0.01	729	9.4 ± 1.2

from 41 μs up to 290 μs with an additional inert shell. Meanwhile, decay times, which are calculated by finding the time it takes after states are fully populated to decrease to 1/e of maximum intensity values, also increase from 101 μs for the core up to 983 μs for Y-shelled UCNPs. The combined lifetime and UCQY measurements suggest that surface quenching is sufficiently reduced in nanoparticles with an inert shell. Interestingly, Gd-shelled samples have shorter decay lifetimes than Lu-shelled samples (643 μs versus 729 μs) despite being more efficient. Opposing QY and lifetime trends suggest that a compressive shell reduces radiative lifetimes and increases the probability for radiative emission. This result supports our hypothesis that the cores in Gd-shelled nanoparticles experience counteracting tensile strain and therefore, local crystal field modifications that alter radiative probabilities. In the SI, we include lifetime curves for other emission states under 980 nm and direct excitation wavelengths, which highlight similar trends.

To probe the mechano-optical properties of the core−shell nanoparticles, we use a laser-coupled diamond anvil cell (DAC) to simultaneously exert pressures from ambient up to ∼5 GPa and monitor upconversion emission under stress. Nanoparticles are loaded in a 295 μm diameter sample chamber with silicone oil as the hydrostatic pressure medium. A bulk ruby sphere is also loaded to provide pressure calibration.[28] For each pressure increment, we collect spectra to calculate the red to green ratio $\left(\frac{I_r}{I_g}\right)$ and digital images to visualize the corresponding color and intensity changes (further details in SI). In this way, we investigate how synthetically strained nanoparticles react optically to external stress. Consistent with our previous study,[4] cubic-phase nanoparticles have enhanced red emission relative to green at higher pressures, because the green intensity decreases more rapidly than red intensity. This effect is seen in the spectra, each normalized to the green peaks, as well as the images of the DAC sample chamber under 980 nm illumination. Figure 4a−c plot representative spectra for the three core−shell types and their corresponding images from the loading (black), maximum (color), and full release (dashed color) pressures. Most evident is the difference in the initial color, which follows the same trend as those in the optical experiments (Figure 3). In particular, the fitted ambient $\frac{I_r}{I_g}$ values for Gd-, Y-, and Lu-shelled UCNPs are 3.98 ± 0.01, 3.49 ± 0.06, and 4.47 ± 0.04, respectively. For nanoparticles with inert Gd and Lu shells, upconversion emission turns from yellow-green or yellow to orange at higher pressures. Meanwhile, nanoparticles with an inert Y shell turn from green to yellow-brown.

In Figure 4d, we track the percent change in the red to green ratio from ambient values $\left(\Delta\frac{I_r}{I_g}\right)$ for three complete cycles of compression and release. Data collected at incremental pressure points follow a positive linear trend. For each cycle, we graph the linear error-weighted least-squares fit of $\Delta\frac{I_r}{I_g}$. The slopes (% per GPa) measure mechanosensitivity, with higher values representing a larger color response to stress. Across three cycles, mechanosensitivity values show no significant decline, highlighting the structural and optical robustness of this system for multiple pressure measurements. Of the three types of core−shell nanoparticles, Gd-shelled UCNPs are the most responsive to external stress with a slope of 12.2 ± 1.2% per GPa. This enhanced response once again suggests that compressive strain in the shell influences the mechanosensitivity of the core by way of a counteracting tensile strain that extends into the core. With external compression that inhomogeneous strain could propagate further into the core and distort the crystal field of active lanthanide ions. Interestingly, the Y- and Lu-shelled samples have similar sensitivity metrics: 9.2 ± 1.0% per GPa and 9.4 ± 1.2% per GPa. Given XRD results in Figure 2 that indicate both a smaller magnitude of strain on the lattice and peak asymmetry, active ions in the cores of Lu-shelled samples are not significantly affected by tensile strain in the shell layer. Most of the strain seems isolated within the shell because stretching is energetically favored over contracting. In fact, we find that these sensitivity values are similar to those of smaller, unshelled cubic-phase nanoparticles at 10.5 ± 1.1% per GPa.[4] Therefore, sensing capabilities, as we have defined them in terms of $\Delta\frac{I_r}{I_g}$, are independent of surface quenching effects. Not only does our shelling strategy successfully mitigate surface quenching and improves QY efficiency, but it also maintains or, in some cases, improves the color response of these upconverters.

In conclusion, we systematically study how strain induced by heteroepitaxial growth modifies optical and mechanical sensing capabilities of core−shell nanoparticles. For reference, characterization measurements are summarized in Table 1. In general, an inert shell of ∼4.5 nm thickness improves the UCQY of sub-25 nm α-$NaYF_4$:Yb,Er cores to >0.1%, a value on par with 30 nm hexagonal-phase cores at the same 150 W/cm^2 irradiance.[23] Of the inert shells, one with minimal lattice mismatch (i.e., $NaYF_4$) yields the largest UCQY enhancement by effectively reducing surface quenching. An unstrained shell does not alter the intrinsic mechanosensitivity of the centrosymmetric cubic-phase lattice, while a compressively strained shell (i.e., $NaGdF_4$) increases the color response to stress. Shelling thus provides a complementary synthetic strategy to expand the upconverting toolkit we presented in earlier work. In that study, we implemented d-metal dopants to tune the mechanosensitivity of cubic- and hexagonal-phase upconverting cores.[4] Adding inert shells to d-metal doped cores could therefore maximize the sensitivity, signal collection, and resolution for measuring forces. Furthermore,

DOI: 10.1021/acs.nanolett.8b01535
Nano Lett. 2018, 18, 4454−4459

heteroepitaxial shelling provides modalities beyond luminescence and mechanical sensing. He et al., for example, utilized $NaLuF_4$ and $NaGdF_4$ as contrast agents in CT and MRI, respectively.[20] $NaGdF_4$ has also been reported to have high stability under an electron beam,[21] providing a protective layer for electron microscopy and cathodoluminescence studies. Ultimately, our results have positive implications for using cubic-phase UCNPs as in vivo and in situ optical sensors and guides future work toward multimodal architectures.

■ ASSOCIATED CONTENT

Supporting Information

The Supporting Information is available free of charge on the ACS Publications website at DOI: 10.1021/acs.nanolett.8b01535.

Methods, results, and further discussion of nanoparticle syntheses, QY, lifetime, DAC, and other characterization (i.e., ICP-OES, TEM, XRD) measurements (PDF)

■ AUTHOR INFORMATION

Corresponding Authors

*E-mail: alay@stanford.edu.
*E-mail: jdionne@stanford.edu.

ORCID

Alice Lay: 0000-0001-5179-7150
A. Paul Alivisatos: 0000-0001-6895-9048

Notes

The authors declare no competing financial interest.

■ ACKNOWLEDGMENTS

The authors thank Arturas Vailionis, Fariah Hayee, Katherine Sytwu, Guangchao Li, Tarun Narayan, Michael Wisser, David Barton III, Jefferson Dixon, Shing Shing Ho, and Yu Lin for feedback and support. A.L., R.D.M., M.B.G., and J.A.D. acknowledge financial support from the Stanford Bio-X Interdisciplinary Initiatives Committee (IIP). A.L. was previously on NSF GRFP (2013156180). C.S. was supported by an Eastman Kodak fellowship. S.F., A.P.A, and J.A.D. acknowledge support from the "Light-Material Interactions in Energy Conversion" Energy Frontier Research Center under Grant DE-SC0001293, funded by the U.S. Department of Energy, Office of Science, Office of Basic Energy Sciences, under contract DE-AC02-05CH11231. S.F. also acknowledges scholarship support from the German Research Foundation (DFG, agreement FI 2042/1-1). Work by F.K. and W.L.M. was supported through the Department of Energy through the Stanford Institute for Materials and Energy Sciences DE-AC02-76SF00515. TEM imaging and XRD characterization were performed at the Stanford Nano Shared Facilities (SNSF), supported by the National Science Foundation under award ECCS-1542152.

■ REFERENCES

(1) Mehlenbacher, R. D.; Kolbl, R.; Lay, A.; Dionne, J. A. *Nat. Rev. Mater.* **2017**, *3*, 17080.
(2) Wang, F.; Banerjee, D.; Liu, Y.; Chen, X.; Liu, X. *Analyst* **2010**, *135*, 1839−1854.
(3) Tsang, M.-K.; Bai, G.; Hao, J. *Chem. Soc. Rev.* **2015**, *44*, 1585−1607.
(4) Lay, A.; Wang, D. S.; Wisser, M. D.; Mehlenbacher, R. D.; Lin, Y.; Goodman, M. B.; Mao, W. L.; Dionne, J. A. *Nano Lett.* **2017**, *17*, 4172−4177.
(5) Wisser, M. D.; Chea, M.; Lin, Y.; Wu, D. M.; Mao, W. L.; Salleo, A.; Dionne, J. A. *Nano Lett.* **2015**, *15*, 1891−1897.
(6) Dong, N.-N.; Pedroni, M.; Piccinelli, F.; Conti, G.; Sbarbati, A.; Ramírez-Hernández, J. E.; Maestro, L. M.; Iglesias-de la Cruz, M. C.; Sanz-Rodriguez, F.; Juarranz, A.; Chen, F.; Vetrone, F.; Capobianco, J. A.; Solé, J. G.; Bettinelli, M.; Jaque, D.; Speghini, A. *ACS Nano* **2011**, *5*, 8665−8671.
(7) Wawrzynczyk, D.; Bednarkiewicz, A.; Nyk, M.; Strek, W.; Samoc, M. *Nanoscale* **2012**, *4*, 6959−6961.
(8) Balabhadra, S.; Debasu, M. L.; Brites, C. D.; Nunes, L. A.; Malta, O. L.; Rocha, J.; Bettinelli, M.; Carlos, L. D. *Nanoscale* **2015**, *7*, 17261−17267.
(9) Klier, D. T.; Kumke, M. U. *J. Phys. Chem. C* **2015**, *119*, 3363−3373.
(10) Wang, Y.-L.; Zhang, J.-P.; Han, J.-B.; Hao, Z.-H.; Wang, Q.-Q. *J. Appl. Phys.* **2015**, *117*, 083903.
(11) Haase, M.; Schäfer, H. *Angew. Chem., Int. Ed.* **2011**, *50*, 5808−5829.
(12) Wang, F.; Wang, J.; Liu, X. *Angew. Chem.* **2010**, *122*, 7618−7622.
(13) Johnson, N. J.; He, S.; Diao, S.; Chan, E. M.; Dai, H.; Almutairi, A. *J. Am. Chem. Soc.* **2017**, *139*, 3275−3282.
(14) Fischer, S.; Bronstein, N. D.; Swabeck, J. K.; Chan, E. M.; Alivisatos, A. P. *Nano Lett.* **2016**, *16*, 7241−7247.
(15) Chen, G.; Shen, J.; Ohulchanskyy, T. Y.; Patel, N. J.; Kutikov, A.; Li, Z.; Song, J.; Pandey, R. K.; Ågren, H.; Prasad, P. N.; Han, G. *ACS Nano* **2012**, *6*, 8280−8287.
(16) Su, Y.; Liu, X.; Lei, P.; Xu, X.; Dong, L.; Guo, X.; Yan, X.; Wang, P.; Song, S.; Feng, J.; Zhang, H. *Dalton Trans.* **2016**, *45*, 11129−11136.
(17) Dong, H.; Sun, L.-D.; Li, L.-D.; Si, R.; Liu, R.; Yan, C.-H. *J. Am. Chem. Soc.* **2017**, *139*, 18492.
(18) Wu, D. M.; García-Etxarri, A.; Salleo, A.; Dionne, J. A. *J. Phys. Chem. Lett.* **2014**, *5*, 4020−4031.
(19) Liu, J.-N.; Bu, W.-B.; Shi, J.-L. *Acc. Chem. Res.* **2015**, *48*, 1797−1805.
(20) He, S.; Johnson, N. J.; Nguyen Huu, V. A.; Cory, E.; Huang, Y.; Sah, R. L.; Jokerst, J. V.; Almutairi, A. *Nano Lett.* **2017**, *17*, 4873−4880.
(21) Johnson, N. J.; van Veggel, F. C. *ACS Nano* **2014**, *8*, 10517−10527.
(22) Smith, A. M.; Mohs, A. M.; Nie, S. *Nat. Nanotechnol.* **2009**, *4*, 56.
(23) Boyer, J.-C.; Van Veggel, F. C. *Nanoscale* **2010**, *2*, 1417−1419.
(24) Li, X.; Liu, X.; Chevrier, D. M.; Qin, X.; Xie, X.; Song, S.; Zhang, H.; Zhang, P.; Liu, X. *Angew. Chem.* **2015**, *127*, 13510−13515.
(25) Peng, X.; Schlamp, M. C.; Kadavanich, A. V.; Alivisatos, A. P. *J. Am. Chem. Soc.* **1997**, *119*, 7019−7029.
(26) Dong, L.; Schnitker, J.; Smith, R. W.; Srolovitz, D. J. *J. Appl. Phys.* **1998**, *83*, 217−227.
(27) Trushin, O.; Granato, E.; Ying, S.; Salo, P.; Ala-Nissila, T. *Phys. Rev. B: Condens. Matter Mater. Phys.* **2003**, *68*, 155413.
(28) Mao, H.; Xu, J.-A.; Bell, P. *J. Geophys. Res.* **1986**, *91*, 4673−4676.

DOI: 10.1021/acs.nanolett.8b01535
Nano Lett. 2018, 18, 4454−4459